

A Framework Nucleic Acid Based Robotic Nanobee for Active Targeting Therapy

Taoran Tian, Dexuan Xiao, Tao Zhang, Yanjing Li, Sirong Shi, Wenyu Zhong, Ping Gong, Zhan Liu,* Qian Li,* and Yunfeng Lin*

DNA nanotechnology has provided new strategies and platforms for cargo delivery. However, DNA-based nanostructures utilized for cargo delivery have mainly focused on static structures and passive targeting. Here, inspired by honeybee's natural reaction to hazards, a melittin loaded tetrahedron framework nucleic acid (tFNA) nanostructure, for active targeting therapy as a "nanobee" is developed. Upon exposure to target proteins on the cell membrane, the tFNA exoskeleton goes through conformation change, leading to the selective release of melittin from the exoskeleton and the consequent selective lethal effect. As a result, the active targeting of the nanobee to tumor cells is achieved. At the same concentrations of melittin, the nanobee exhibits significantly higher and more selective cytotoxicity against target cells than free melittin molecules, whereas the inactive nanobee shows neglectable lethal effect. Notably, the complete encapsulation of melittin in the tFNA exoskeleton is confirmed by the combination of experimental screening and molecular dynamic analysis, which is proposed to be the origin of the minimized off-target effects of nanobee. This nanobee concept offers a strategy that may be extended to various dynamic stimuli-responsive cargo delivery systems, to enhance cargo stability and decrease severe off-target effects.

1. Introduction

Nanodevices based on nucleic acid structures offer advantages over other counterparts when serving as cargo delivery devices, such as highly precise and predictable structures originated from self-assembly following the Watson-Crick base pairing rule, and low toxicity owing to their biocompatible nucleic acid nature.^[1] Among these, framework nucleic acid (FNA) structures are a group of DNA nanostructures characterized by a framework morphology. Merited with simple fabrication and high yield, FNA structures have been applied in various biomedical applications.^[2] It has been demonstrated that FNA structures have enhanced capabilities for cellular uptake and tissue penetration, thus could serve as potent candidates for cargo delivery.^[1a,2b,3] Albeit FNA structures have been used as carriers for years, they were mainly applied in the static and passive forms.^[4] The dynamic

and active targeting strategies were much less reported in applications, apart from FNA based biosensors with different fluorescence pair modifications.^[2a,c]

Comparing to static structures, to achieve a dynamic stimuli-responsive delivery requires a more delicate design. It is critical to achieving cargo encapsulation for inactive vehicles, which serve as shelters to protect cargos until activated by specific triggers. For example, Li et al. first applied the dynamic stimuli-responsive delivery strategy in vivo with a DNA origami-based tube to achieve thrombin encapsulation and delivery. In their approach, thrombin is loaded onto a DNA origami sheet, which would be rolled into a tube and locked by an aptamer switch to achieve active targeting.^[5] Contrary to rigid DNA origami structures, FNA structures generally consist of short DNA strands, providing less spatial confinement to the encapsulated cargos. Regarding the limited spatial confinement and spiral nature of DNA helix, it is critical to optimize the cargo loading site for the best encapsulation. While various solid DNA origami structures (tube,^[5] box,^[6] sphere^[7]) have been reported to achieve cargo encapsulation easily, determining the loading site is of particular importance when applying FNA to control cargo drug/enzyme activity.^[8]

To apply FNA for dynamic and active cargo delivery, we took inspirations from the honeybee's natural reaction to hazards. Venom is safely carried by honeybees under common conditions,

T. Tian, D. Xiao, Dr. T. Zhang, Y. Li, Dr. S. Shi,
Prof. P. Gong, Prof. Y. Lin
State Key Laboratory of Oral Diseases
National Clinical Research Center for Oral Diseases
West China Hospital of Stomatology
Sichuan University
Chengdu, Sichuan 610041, China
E-mail: yunfenglin@scu.edu.cn

Dr. W. Zhong, Prof. Z. Liu
Key Lab for Biomechanical Engineering of Sichuan Province
Sichuan University
Chengdu, Sichuan 610065, China
E-mail: zhanliu@scu.edu.cn, bmeliuzhan@163.com

Prof. Q. Li
School of Chemistry and Chemical Engineering
Frontiers Science Center for Transformative Molecules
Institute of Translational Medicine
Shanghai Jiao Tong University
Shanghai 200240, China
E-mail: liqian2018@sjtu.edu.cn

Prof. Y. Lin
College of Biomedical Engineering
Sichuan University
Chengdu, Sichuan 610041, China

 The ORCID identification number(s) for the author(s) of this article can be found under <https://doi.org/10.1002/adfm.202007342>.

DOI: 10.1002/adfm.202007342

and released when honeybees perceive dangers and react in defensive response. In our biomimetic approach, we encapsulate melittin (MLT), the main component of honeybee venom, in a tetrahedral FNA (tFNA) exoskeleton to fabricate a robotic nanobee, which can perceive and respond to target cells. To select the best cargo loading sites for MLT encapsulation, we applied experimental screening together with all-atom MD analysis. At the selected loading position, MLT molecules could be well-encapsulated by the tFNA exoskeleton, and thus could not interact with the outer environment until the decomposition of the tFNA exoskeleton was triggered by specific stimuli. To mimic the honeybee's defensive reaction to hazard, we employed an aptamer sequence AS1411 into the tFNA exoskeleton, to serve as a stimuli-responsive unit. When binding to cell membrane nucleolin, the conformation change of AS1411 would result in the decomposition of the tFNA exoskeleton, and consequently the release of encapsulated MLT. The MLT release through this dynamic and stimuli-responsive opening of the tFNA exoskeleton is similar to honeybee's stimuli-responsive and self-contained sting, therefore, we denoted this dynamic stimuli-responsive delivery system as nanobee (Figure 1). This concept can be extended for targeted delivery of various molecules, to enhance cargo stability and decrease severe off-target effects.

2. Results and Discussion

2.1. Design and Fabrication of the Stimuli-Responsive tFNA Exoskeleton

To support and encapsulate cargo MLT, we selected a tFNA as the base structure for its convenient fabrication, excellent biocompatibility, and good tissue penetration ability.^[1a]

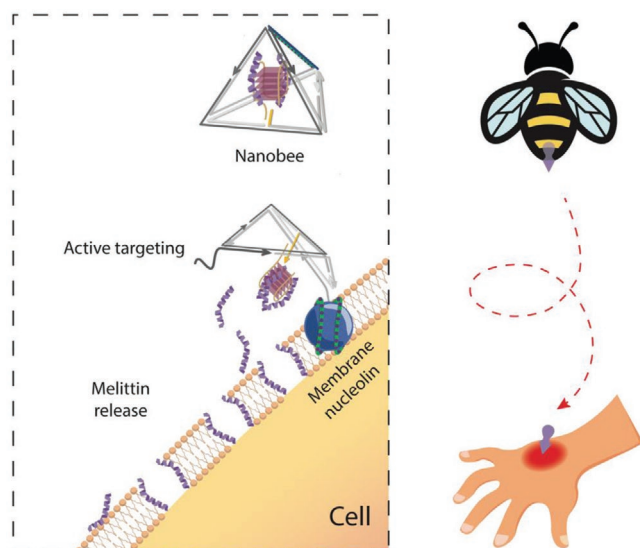


Figure 1. The tFNA-based nanobee for active targeting therapy, inspired by the honeybee's natural reaction to hazards. In a nanobee, melittin (MLT) molecules are encapsulated and protected by the tFNA exoskeleton. Upon exposure to nucleolin on the cell membrane, the tFNA exoskeleton is decomposed and MLT molecules are released then penetrate the cell membrane, like the sting by a honeybee on human skin.

The tFNA exoskeleton was initially designed using Tiamat and Cando as reported previously (Figure 2A; Table S1 and Figure S1, Supporting Information).^[9] Briefly, a tetrahedron structure with six 32 base pair (bp) edges was formed with single strands. For targeting membrane nucleolin, we introduced the AS1411 aptamer sequence into one strand (beginning at the 5' end of strand #5, Table S1, Supporting Information).^[10] For cargo loading, we assigned a nick on the edge opposite to the switch edge (loading edge, Figure 2A). The design was tested via one-pot annealing and verified by gel electrophoresis, the yield of the tFNA exoskeleton was determined to be $\approx 95.6\%$ (Figure S2B, Supporting Information).

To examine the stimuli-responsive function of the primary tFNA exoskeleton, we employed fluorescein (FAM) and black hole quencher-1 (BHQ-1). Three versions of tFNA exoskeletons in two different states (open or close, Figure 2B), by modifying FAM at the 5' end of AS1411 located on the #5 strand alone (tFNA-F) or together with BHQ-1 at the 3' end of strand #6 to form a closed tFNA structure (tFNA-F/B-C). We verified that of similar mobilities in polyacrylamide gel electrophoresis (PAGE), FAM fluorescence of the BHQ-1-modified tFNA exoskeleton was quenched, indicating that the exoskeleton was in the "off" mode (switch closed) (Figure 2B and Figure S2C, Supporting Information). Conversely, the open tFNA exoskeleton (tFNA-F/B-O, via removing strand #7) could partially restore fluorescence by elongating the distance between two fluorescence molecules (Figure 2B and Figure S2D, Supporting Information). These results set a benchmark for the following investigations.

To achieve successful MLT encapsulation and dynamic release, it is important to keep the free energy of the switch edge strand hybridization within a window that can facilitate exoskeleton fabrication and de-hybridization upon encountering the target.^[5] To figure out the optimum energy window, we extracted the switch edge out of the exoskeleton structure and compared three different strand #7 designs (strand #5 stays the same as it provides the AS1411 sequence). These three designs have 29, 24, and 15 bases paired to the AS1411 strand, respectively, endowing three different free energies when hybridized with the AS1411 aptamer.^[11] (Figure S3A-C, Supporting Information) To determine whether these strands could be de-hybridized by nucleolin, we modified FAM to the 5' end of AS1411 and BHQ-1 to the 3' end of three complementary strand designs (Figure S3D, Supporting Information). We first verified the quenching efficiency of different designs by using a fluorescence spectrophotometer (Figure S3E, Supporting Information), and then flow cytometry was applied to examine the switch-on function. Briefly, a documented membrane-nucleolin positive cell line (HUVECs), was cultured and exposed to different switches for 2 h; the cells were then collected by scraping and analyzed by fluorescence detection (Figure S4A, Supporting Information).^[5] As expected, if more bases were paired in the switch design, less fluorescence would be restored: C15 design resulted in $\approx 30.9\%$ of fluorescence-positive cells, which was similar to single-stranded FAM-labeled AS1411 ($\approx 33.9\%$, Figure S4, Supporting Information). Notably, when cells were collected via trypsin digestion, which damages membrane proteins, no group had a positive count, indicating the fluorescence observed after scraping

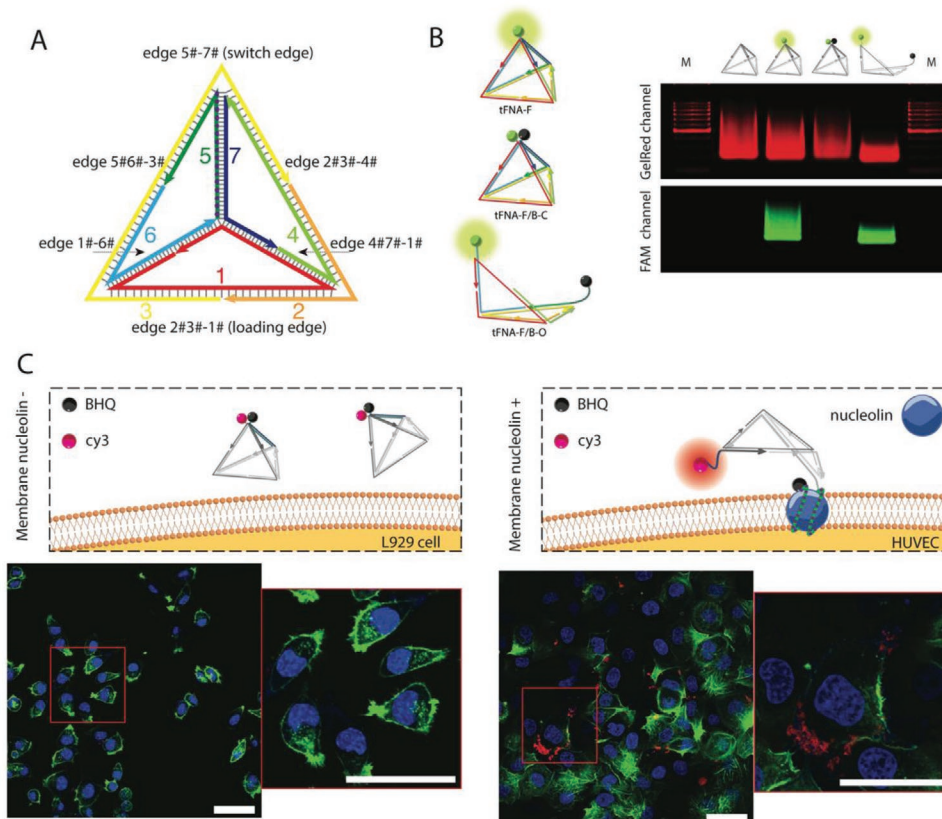


Figure 2. Design and fabrication of the dynamic tFNA exoskeleton. A) Diagram of the dynamic tFNA structure design. Six edges were named after the compositional strands. The arrow indicates the 5'-3' direction. Purple dot represents the AS1411 sequence. B) tFNA exoskeletons in different states verified by gel electrophoresis with fluorescence. (green sphere: FAM, black sphere: BHQ-1) C) Laser confocal microscopic observation of cy5/BHQ-1-modified tFNA exoskeleton (tFNA-cy5/B) confirmed the targeted conformation changeability, for that membrane nucleolin positive cells (HUVECs) could help tFNA-cy5/B restore cy5 fluorescence, whereas tFNA-cy5/B stayed quenched when incubated with membrane nucleolin negative cells (L929 cells). Scale bar, 50 μm .

was triggered by membrane-located nucleolin (Figure S5, Supporting Information). Thereafter, we selected the C15 switch to fabricate the FAM/BHQ-1-labeled tFNA exoskeleton (tFNA-C15) for further investigation. We applied the tFNA-C15 in addition to the C15 switch to HUVECs. Flow cytometry suggested that the positive count rate of tFNA-C15 was between the C15 switch and the negative control (Figure S6, Supporting Information). This might result from the limited spatial distance between FAM and BHQ-1 molecules linked to the opened tFNA exoskeleton.

To verify the targeting ability, we applied a Cy5/BHQ-1-labeled tFNA (tFNA-cy5/B) incubating with these cells. This fluorescence-modified tFNA exoskeleton stayed partially quenched until the AS1411 strand detached and opened the structure (Figure S7, Supporting Information). The confocal images showed that, compared with L929 cells (w/o membrane nucleolin), HUVECs tended to intensely trigger conformational changes in the nanobee and exhibited stronger fluorescence signals (Figure 2C and Figure S8, Supporting Information). Besides, we found that the single-strand AS1411 aptamers showed a certain degree of "stickiness" as they bound to L929 cells and HUVECs nonspecifically (Figure S8, Supporting Information). This observation implied that a single-strand

aptamer-targeting strategy may encounter nonspecific binding and cause off-target drawbacks.^[12]

So far, we acquired a tFNA exoskeleton with dynamic stimuli-responsive ability. The switch edge embedded tFNA was then built virtually for all-atom MD analysis, which verified a stable tetrahedron structure in the process of equilibrium, and the switch edge was the most vulnerable site for de-hybridization in the exoskeleton (Figure S9 and Movie S1, Supporting Information).

2.2. Optimization of Cargo Encapsulation

Unlike rigid DNA origamis, FNA structure could only provide a limited barrier. Therefore, the cargo-loading position at FNA is crucial for cargo delivery. Considering the spiraling nature of DNA helix, we firstly referred to Turberfield's previous study and screened candidate sites.^[13] We attached a 24 nucleotides (nt) hairpin lagging tag to sites continuously on the loading edge, the spiraling nature of DNA endowed different trajectories to the lagging tag, thus changing the mobility of the tFNA exoskeletons in gel electrophoresis. The tFNA exoskeleton with the lowest mobility resistance was then selected for the following

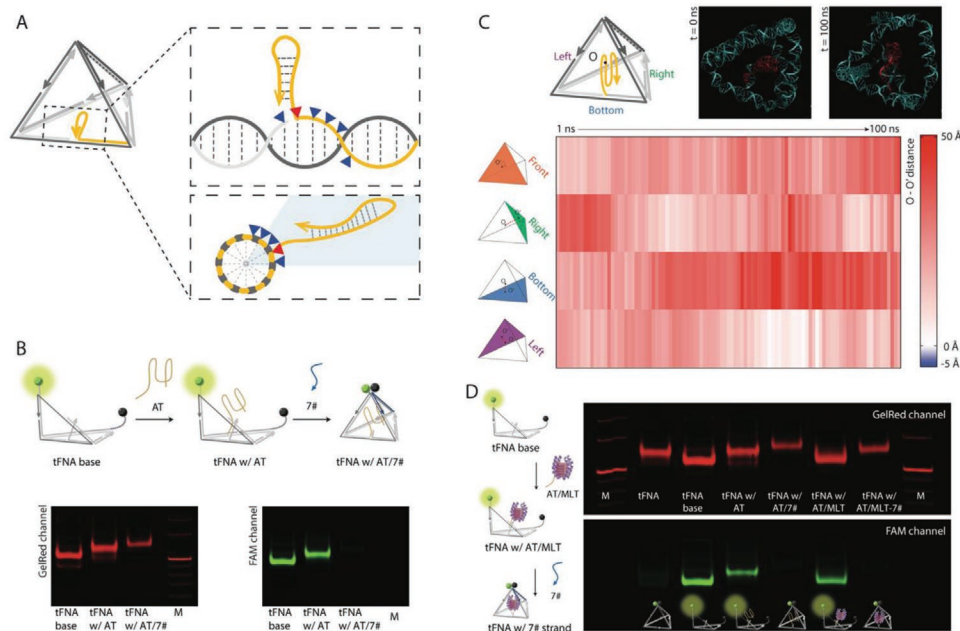


Figure 3. Cargo encapsulation optimized with experimental screening and all-atom MD simulation. A) Continuous sites were screened for cargo loading via PAGE gel electrophoresis (screened sites are denoted as blue triangles). The best loading site (shown in the panel, red triangle) was selected by lagging tag modification (yellow loop at 3'end). B) The cargo loading strand (attachment strand, AT strand) was loaded into the exoskeleton with stepped annealing: the green sphere represents the 3' modification of FAM, the black sphere represents the 5' modification of BHQ-1. The fluorescence changes and band shifts in PAGE gel indicated successful fabrication of the AT strand loaded tFNA exoskeleton. C) All-atom MD simulation of the AT strand loaded tFNA exoskeleton revealed the AT strand being well-encapsulated inside the tFNA exoskeleton. The distances between the center of mass of the G-quadruplex strand (O) and the four surfaces of the tFNA (O-O') were calculated to be positive during the equilibrium state. D) Fabrication of MLT-loaded tFNA exoskeleton, the nanobee, was realized via three-step annealing and verified by PAGE gel electrophoresis.

experiments, as the lagging tag modified at that site was pointed to the most inward trajectory to the middle of the tFNA exoskeleton. (Figure 3A and Figures S10,S11, Supporting Information).

To achieve a minimalist design and fabrication, we applied a DNA G-quadruplex strand as the scaffold to bind MLT for cargo encapsulation. Rich in guanine, a G-quadruplex strand could self-fold into layers of G-tetrads via Hoogsteen hydrogen bonding with the help of cations.^[14] Furthermore, the G-quadruplex structure has been discovered with various cargo binding mechanisms, such as groove docking and hydrogen bonding,^[10a,15] which could boost the loading capacity. Moreover, the inner cavity of the tFNA exoskeleton was limited, the G-quadruplex structure could be self-folded into a dense, negatively charged “core” to maximize the cargo binding without penetrating the exoskeleton.

We selected one G-quadruplex attachment strand (AT strand) among four alternatives to achieve MLT loading (Table S1 and Figures S12-S13, Supporting Information). A three-staged annealing procedure was applied for fabrication (Figure 3B). To verify the fabrication, the aforementioned FAM/BHQ-1 fluorescence pair was applied. The fluorescence intensity and gel electrophoresis suggested satisfying fabrication of the AT strand loaded tFNA exoskeleton (Figure 3B and Figure S13, Supporting Information).

Having experimentally determined the optimized cargo loading site, we further applied all-atom MD analysis to determine whether the AT strand could be encapsulated well as the model cargo in the process of equilibrium. Briefly, we loaded the predetermined AT strand into an all-atom tFNA model to

examine the encapsulation during the equilibrium state, with the AT strand loading site and sequence of the tFNA exoskeleton model identical to our previous experiments. MD results indicated that the shape of the tFNA exoskeleton loaded with the AT strand was almost identical with that without loading, suggesting the exoskeleton integrity is not affected (Figure 3C and Figure S14, Supporting Information). The maximum fluctuation of the G-quadruplex strand relative to the initial position was 3.27 nm during the equilibrium state (Figure S14, Supporting Information). The inner volume of the tFNA exoskeleton fluctuated between 120.9 and 209.8 nm³, providing sufficient cavity for small cargos such as MLT, which has a dimension of ≈40 Å. Most importantly, the AT strand was observed to be encapsulated well in the tFNA exoskeleton during the equilibrium state (Movie S2, Supporting Information). We quantified the encapsulation by measuring the distances between the center of mass of the AT strand (O) and the four surfaces of the tFNA exoskeleton. As shown in Figure 3C, all measurements kept positive during the equilibrium state, indicating the experimentally determined cargo loading site could support the AT strand locating at the center of the tFNA exoskeleton, and the encapsulating persists in the simulation. Taken together, the combination of experiments and MD analysis confirmed the complete encapsulation of MLT in the tFNA exoskeleton.

The MLT loaded tFNA exoskeleton, so-called nanobee, was finally fabricated via a staged approach. First, MLT and the AT strand were incubated overnight at room temperature. The stable binding between MLT and AT strand was demonstrated

by PAGE analysis shown in Figure S15B (Supporting Information). After purification, the estimated MLT/AT strand ratio was 2.29 ± 0.98 , as determined by UV absorption (Figure S15C, Supporting Information). Subsequently, the MLT/AT core was applied to the tFNA base with a three-stage annealing protocol (Figure 3D and Figure S16A, Supporting Information). Gel electrophoresis and fluorescence spectrophotometry verified that the AT/MLT complex could participate and ensure the successful fabrication of the nanobee (Figure 3D and Figure S16B,C, Supporting Information).

2.3. Therapeutic Evaluation of the Nanobee

As described above, the AS1411 strand was utilized as the targeting domain, because it could recognize and bind nucleolin

specifically. Considering the nucleolin level at the membrane varies from cell to cell, the MLT could grant a direct membrane targeting and effecting strategy. As the major component of honeybee venom, MLT can disrupt phospholipid packing in membrane structures and therefore damages cells and tissues indiscriminately by pore forming.^[16] Its cell-penetrating and cytotoxic effects have been applied mainly to fabricate non-viral delivery vectors^[17] and MLT-combination drug delivery systems.^[18] After the successful tFNA exoskeleton design and MLT encapsulation, the nanobee was expected to have the honeybee-mimic behavior, that is, stimuli-responsive MLT release (Figure 4A). We would evaluate this active MLT delivery in vitro and in vivo.

First, cells with different membrane nucleolin expression levels were selected for in vitro experiments. The mouse fibroblast cell line, L929 cell, was chosen as the negative control,

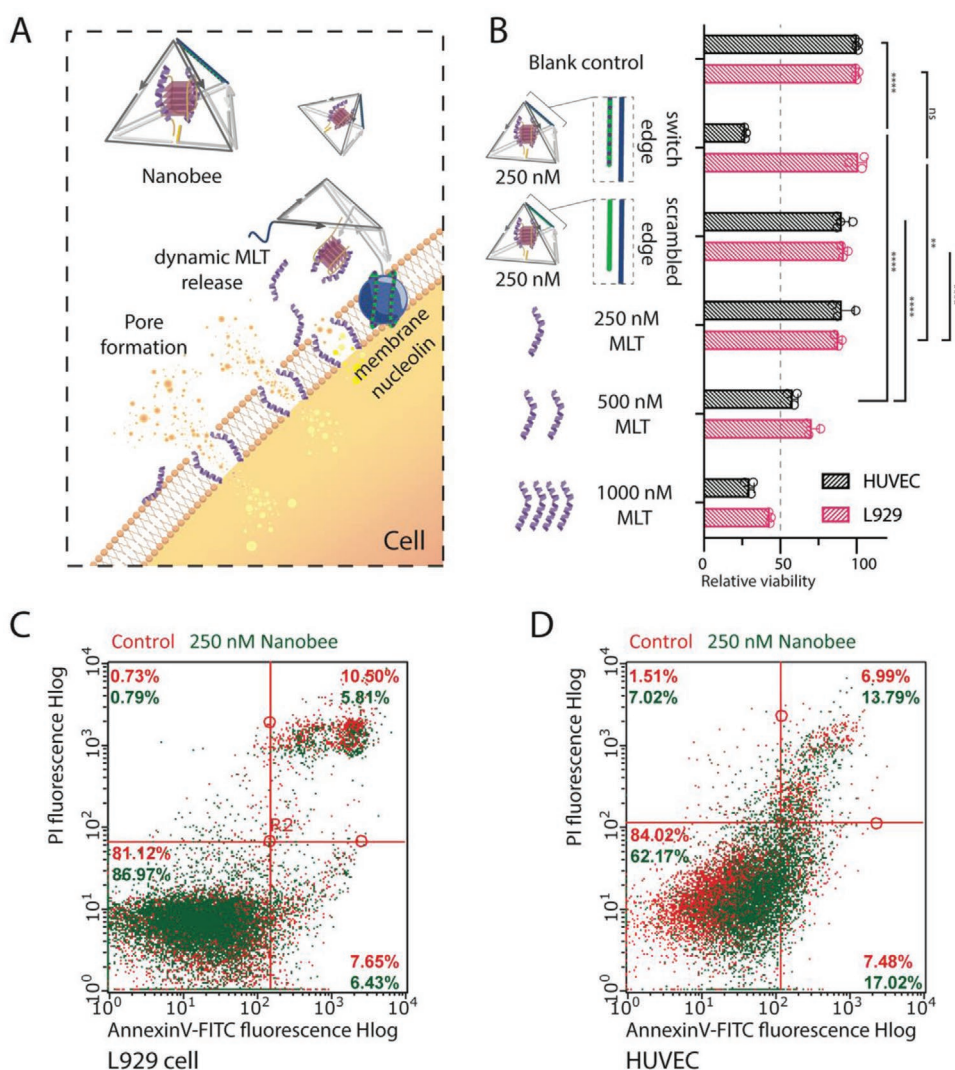


Figure 4. In vitro evaluation of the nanobee. A) Schematic illustration of the working principle of nanobee. Dynamic MLT release was triggered on the membrane of nucleolin-positive cells (HUVECs), leading to pore formation on the cell membrane and the consequent cell death. B) The CCK-8 assay revealed that 250×10^{-9} M nanobee exerted similar toxicity to HUVECs as 1000×10^{-9} M MLT, whereas inactive nanobee and incubation with L929 cells resulted in limited cytotoxicity. The cell apoptosis assay also indicated that 250×10^{-9} M nanobee triggered less cell apoptosis in C) L929 cells than in D) HUVECs. (**** $P < 0.0001$; ** $P < 0.01$; * $P < 0.05$; ns, no significant difference).

and HUVECs were chosen for their documented high-level expression of membrane nucleolin.^[5,10b,19] Considering that the different cell lines should have different sensitivities to toxins, we compared the cytotoxicity of the nanobee to MLT titration as control. 250×10^{-9} M nanobee was applied for the documented biocompatibility of the tFNA exoskeleton.^[1a,2e] As measured by CCK8 assay and microscopic observation, MLT was toxic to cells in a concentration-dependent manner. Cells began to shrink immediately after exposure to MLT, owing to the membrane destabilization and the subsequent changes in osmotic pressure. 500×10^{-9} M MLT posed significant cytotoxicity to two cells indiscriminately (Figure 4B and Figure S17, Supporting Information). While MLT deformed cells extensively, the nanobee appeared to be able to selectively target the membrane of nucleolin-positive HUVECs. As shown in Figure 4B, 250×10^{-9} M nanobee posed neglectable toxicity against L929 cells ($101.1 \pm 5.5\%$ relative viability compared with the blank control). In contrast, 250×10^{-9} M nanobee was highly toxic to HUVECs ($27.03 \pm 0.64\%$ relative viability), which was comparable to 1000×10^{-9} M MLT ($29.92 \pm 2.94\%$, $P > 0.05$). Moreover, when the decomposition of the tFNA exoskeleton is disabled by replacing the switch edge with a base-paired scrambled edge, the inactive nanobee showed significantly decreased cytotoxicity against HUVECs, with $90.3 \pm 5.0\%$ relative viability remained (Figure 4B). The enhanced cytotoxicity of the nanobee might be ascribed to that multiple MLTs were loaded into one nanobee, condensed MLT could facilitate membrane pore formation.^[20]

The cell-specific cytotoxicity of nanobee was further verified by cell apoptosis analysis. Briefly, L929 cells and HUVECs were incubated for 2 h in the presence of culture medium, 250×10^{-9} M nanobee, and 2000×10^{-9} M MLT, respectively, then stained with Annexin V/PI, and analyzed by flow cytometry. In the aforementioned experimental conditions, L929 cells were more sensitive to MLT treatment, as more marker signals were detected, indicating an increase in amounts of apoptotic cells induced by 2000×10^{-9} M MLT (Figure S18, Supporting Information). On the contrary, the treatment with 250×10^{-9} M nanobee resulted in a different pattern, that L929 cells remained healthy (Figure 4C), while a significant level of apoptosis occurred in HUVECs (Figure 4D). This finding was concordance with the results of the CCK-8 assay, suggesting the cytotoxicity of MLT could be modulated by encapsulation in the tFNA exoskeleton, which was selectively decomposed upon exposure to nucleolin on the cell membrane.

We further investigated the therapeutic value of this nanobee system in a human malignant melanoma xenograft mice model. Saline, MLT solution, and nanobee solution were intravenously injected into A375 cells (human malignant melanoma) xenografted nude mice, separately (Figure 5A). The active toxicity of nanobee to A375 cells was verified via CCK-8 assay (Figure S19, Supporting Information). The mice treated with the nanobee exhibited significant tumor growth inhibition. Compared with the administration of saline and MLT solution, the nanobee suppressed the malignant melanoma xenografted tumor growth to $\approx 50\%$, but did not affect mouse weight (Figure 5B–D). The tissue sections revealed that the administration of nanobee could significantly trigger liquefaction necrosis in tumor tissues (Figure 5E). Besides, the systemic administration of MLT exhibited severe off-target damage, causing intense

pathologic changes in the spleen, although the targeting ability of the nanobee appeared to reduce the toxicity of MLT to vital organs (Figure 5E and Figure S20, Supporting Information).

Taken together, the in vitro and in vivo experimental results confirmed that the stimuli-responsive tFNA exoskeleton-based nanobee could act as a drug delivery system, delivering and preserving the bioactivity of encapsulated MLT. The selective MLT release could be achieved via dynamic conformation change of the tFNA exoskeleton triggered by membrane nucleolin. This delivery strategy can be applied to various pre-established membrane protein-aptamer-targeting drug combinations.^[21] It is worth noting the tFNA exoskeleton might have influence on the cell viability. However, that influence should be trivial for the nanobee system. The MLT introduced acute cytotoxicity, while DNA's influence should be exerted in a much longer time scale.^[2e]

3. Discussion and Conclusions

Although DNA nanostructures (such as DNA origami, spherical DNA structures) had established benchmarks for DNA structure-based drug delivery,^[5,22] the FNA structure has potent potential comparing to its counterparts with advantages including: 1) enhanced tissue-penetrating and cellular uptake ability;^[2b] 2) generally greater resistance to biological environments, such as low salt concentrations;^[23] 3) exclusion of viral DNA sequences from preparation and application;^[2d] 4) facile preparation in high yields.^[2e] Previous studies on FNA-based cargo delivery cherished these merits and achieved success in various applications, such as DOX delivery, siRNA delivery, etc.^[24] Whereas their application mainly utilized the FNA structures in static and passive forms, and the potentials of FNA structures need further exploration. The major hinder for utilizing dynamic and active FNA structures for delivery is probably the incomplete cargo encapsulation in the FNA scaffold, resulted from the inability to precisely locate the cargo at the optimal loading site.

To address these issues, we applied experimental screening with the all-atom MD simulation to optimize the cargo encapsulation. These analyses together confirmed a complete encapsulation of MLT in a closed tFNA exoskeleton. Our investigation further verified the MLT encapsulation and the active release upon the stimuli-responsive conformation change of the exoskeleton and addressed the editable and multi-functional nature of FNA structures. The combination of experimental screening with MD verifications is of practical value to various DNA structures demanding precisely spatial control, such as enzyme activity regulation and biomimetic structure construction.

In addition, the honeybee inspired nanobee, MLT loaded dynamic tFNA exoskeleton, set a practical example for how small molecules with severe off-target effects could be safely applied with the help of targeting exoskeleton encapsulation. Our dynamic stimuli-responsive tFNA exoskeleton provides a platform for various potent molecules with pleiotropic effects. This concept can be further extended to targeting delivery of various molecules with a short half-life and/or severe off-target effects.

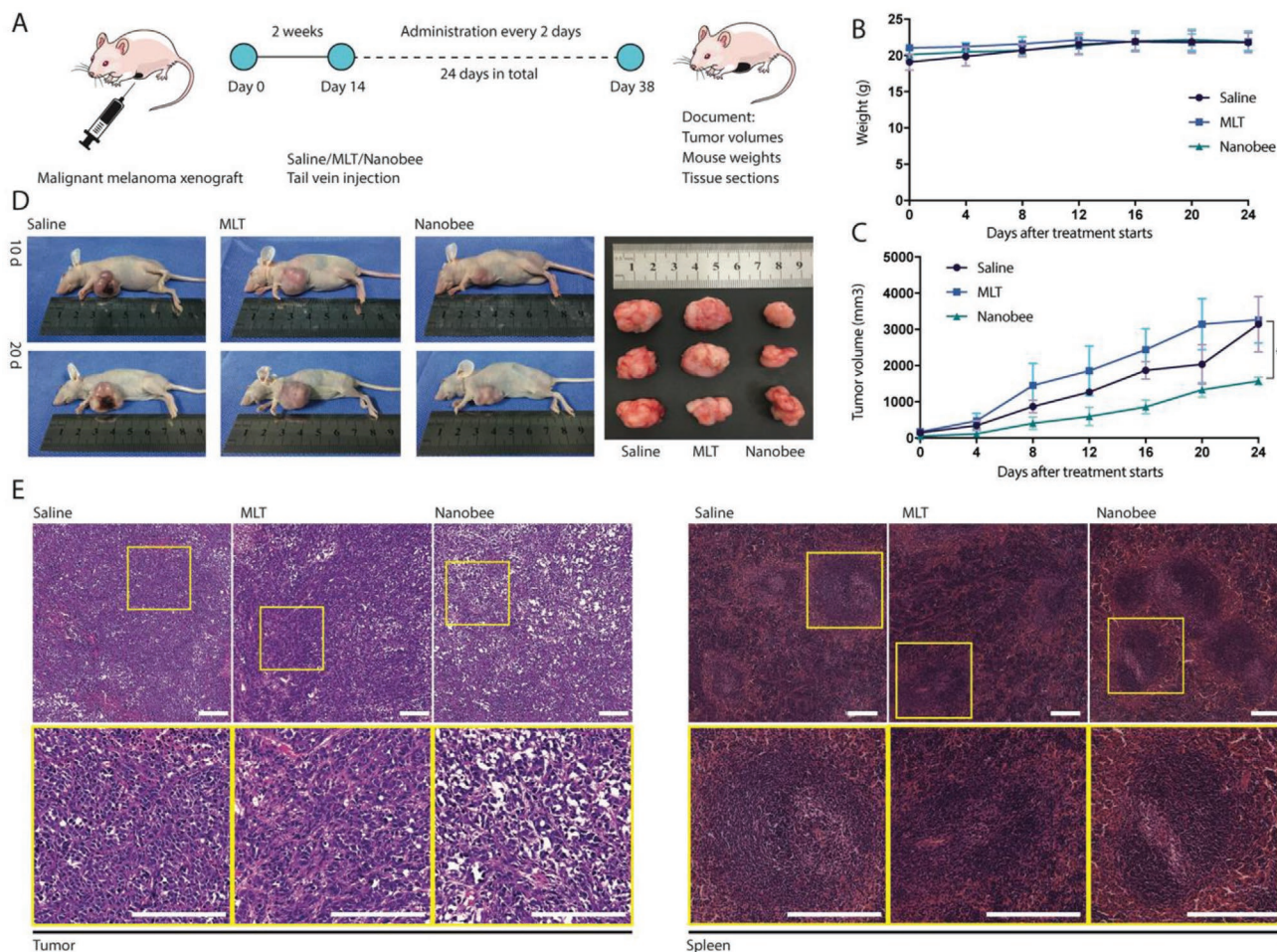


Figure 5. Therapeutic evaluation of the nanobee system. A) A human malignant melanoma (A375) xenografted tumor-bearing mice model was applied to assess the tumor-targeting ability of the nanobee. B–D) After 24 days' treatment, the administration of the nanobee significantly inhibited the growth of the tumor, but had little influence on mouse weight. E) HE staining of the tumor and spleen further revealed the occurrence of intense liquefaction necrosis after nanobee treatment and severe spleen damage caused by the pleiotropic effects of the administration of MLT. The scale bars represent 200 μm . * $P < 0.05$.

4. Experimental Section

Design and Fabrication of the tFNA Exoskeleton: Tiamat (version alpha) was used to design the primary tFNA exoskeleton structure. A nucleolin-targeting AS1411 aptamer sequence was filled manually, beginning at the 5' end of strand #5 (Figure 1A, the green line with the purple dot represents the AS1411 sequence). The rest of the sequences were filled with random bases. All designed DNA oligos were purchased from Sangon Biotechnology. The tFNA exoskeleton fabrication was achieved via one-pot annealing. All required oligos were mixed into TM buffer (10×10^{-3} M Tris, 10×10^{-3} M MgCl_2) at final concentrations of 1×10^{-6} M. The annealing was performed using a PCR thermal cycler (ABI, GeneAmp, PCR system 9700), starting at 95 °C for 10 min and then decreased to 4 °C at maximum ramp speed. The acquired products were purified by Amicon 30 kDa 0.5 mL tubes (Amicon Ultra 0.5 mL, 30K, cat. no. UFC503096) or HPLC according to Xing's protocol using an SEC column (BioSec-SEC-S2000, Henomenex, cat. no. 00H-2145-K0) and used in the subsequent experiments.^[25]

Fluorescence Verification: To verify whether tFNAs were fabricated in a closed state, a FAM/BHQ-1 fluorescence pair was used. The FAM molecule was modified to the 5' end of strand #5, and the BHQ-1 molecule was modified to the 3' end of strand #6. As the 5' end of strand #5 and the 3' end of strand #6 are designed to share the same tetrahedron apex, BHQ-1 should quench FAM if strand #5 and strand #7

are folded correctly. tFNA exoskeletons were fabricated with and without strand #7 using the aforementioned protocol and their fluorescence were measured using a flow cytometer (Beckman, FC500).

Flow Cytometry Testing Switch Designs: The nanobee system must achieve in situ loading delivery. Therefore, successful switch design must satisfy two criteria: 1) the binding between AS1411 and the complementary strand is strong enough to maintain structural integrity, and 2) the binding between AS1411 and the complementary strand is weak enough to allow target sensitivity upon nucleolin exposure. To achieve these criteria, the switch edge was extracted from the tFNA structure and strand replacement abilities were verified using three different complementary strand designs. The switch strands designs were created using the Nupack platform.^[11] The shortest strand had 15 bases paired with AS1411, which was equal to Li's previous final switch design;^[5] the second design had bases paired at intervals to cover the full-length of the AS1411 strand, predicted to have 24 base pairs in total when incubated at 37 °C with AS1411; the longest strand covers the full-length of the AS1411 aptamer and had 29 bases paired. FAM was modified at the 5' end of AS1411 and BHQ-1 was modified at the 3' end of the C15, C24, and C29 strands separately. The annealing of AS1411 and the different complementary strands was performed using the same protocol as for tFNA exoskeleton fabrication. FAM quenching efficiency was verified using a Varioska LUX multimode microplate reader (Thermo Scientific, VL0L0TD0).

HUVECs were purchased from Gempharmatech Co., Ltd. (Nanjing, China) and incubated in a humidified atmosphere with standard conditions (10% fetal bovine serum, 100 U mL⁻¹ penicillin/streptomycin (Hyclone, cat. no. SV30010), 5% CO₂, 37 °C) before they were seeded in 6-well plates at a density of 2 × 10⁵ cells per well. The cells were equilibrated in 0% FBS for 1 h and 250 × 10⁻⁹ M of the annealed AS1411-complementary strand pairs were then added, incubated for 2 h at standard condition, and then collected by cell scraping or trypsin digestion (0.25% w/v trypsin-ethylenediaminetetraacetic acid, Solarbio, cat. no. T1350). The FAM fluorescence-labeled cells were then detected by a flow cytometer (Beckman, FC500).

Fluorescence Observation of Nanobee-Cell Interaction: A different fluorescence pair was used to avoid nonspecific cellular 488 nm laser excitation and emission. Cy5 was modified on the 5' end of strand #5, and the 3' end retained the BHQ-1 modification. The fluorescent nanobee was then fabricated with a one-pot annealing protocol. The quenching efficiency of BHQ-1 was measured via Varioska LUX multimode microplate reader (Thermo Scientific, VL0L0TD0). HUVECs and L929 cells were prepared and seeded into 35 mm glass-bottomed dishes (Nest Biotechnology, cat. no. 801 001), and then incubated overnight in standard conditions. After equilibration in 0% FBS for 1 h, the cells were treated with 250 × 10⁻⁹ M cy5/BHQ-1 nanobee. After incubation for 2 h, the cells were fixed with 4% w/v paraformaldehyde solution (Biosharp, REF. BL539A) and stained with FITC-labeled phalloidin (Cytoskeleton Inc., cat. no. PHDG1) and DAPI (4',6-diamidino-2-phenylindole, Sigma-Aldrich, cat. no. D8417-5MG). The fixed cells were then observed by using a laser confocal microscope (Leica, TCS SP8). To observe the dynamic fluorescence change, the cells were transferred to a microscope camera (Leica, DFC7000 T) upon the addition of fluorescence-labeled nanobee.

Loading Site Screening via Lagging Tag Modification: A lagging tag (5'-3': TTCCCCAAAATTTTTGGGGG) was extended to the 3' end of different #2 strands. It was predicted by Nupack that this tag could form a stable loop structure. For each design, the #3 strand was extended or shortened accordingly to fully match the #1 strand. After self-assembly with other strands, the samples were loaded for PAGE. A typical process consisted of a 5% PAGE, with electrophoresis performed at 80 V for 120 min, and 1 × TBE (diluted from 10 × TBE stock solution, Sangon Biotech, cat. no. B548102) as the running buffer. The nucleic acids were stained with GelRed (Biotium, cat. no. 41 003) according to the manufacturer's instruction and then observed using a ChemiDoc MP Imaging System (Biorad, cat. no. 12 003 154). The DNA size marker applied was 200 bp DNA Ladder (Tiangen Biotech, cat. no. MD115), unless otherwise stated.

MD Analysis: MD was used to investigate the mechanical characteristics of the tFNA exoskeleton. Two all-atom models were built and presented in VMD 1.93 (Visual Molecular Dynamics).^[26] The primary tFNA exoskeleton with a DNA double helix comprised 11 806 atoms, together with 102 710 water molecules, which was named as Model 1. This consisted of 320 301 atoms, showing as a charge-neutral cube with sides of ≈147 Å (Figure S9A,B, Supporting Information). Periodic boundary conditions were applied to simulate an infinite solution environment. A sticky end with a G-quadruplex loading strand d(TGGGGGT)₄ was attached on strand #2 in Model 1 and placed inside the tFNA exoskeleton; this was assigned as Model 2 (Figure S14A, Supporting Information). This consisted of 317 485 atoms, including 13 202 nucleic acid atoms from 415 bases, 101 292 water molecules, and 407 K⁺ ions. Targeted MD was used for the preparation of the simulation to achieve the forcible fold of the G-quadruplex (Figure S14B, Supporting Information). All models were charged neutral. Energy minimization and MD relaxation (longer than 5 ns in total) in NVT or NPT ensembles were repeated with progressively decreasing restraints on the nucleic acids. The dimensions of the two models were ≈147 Å × 147 Å × 147 Å, whereas the dimensions of the tFNA exoskeleton structure were ≈135 Å × 135 Å × 135 Å. Productive simulations up to 100 ns were thus performed in NPT ensembles for the models.

All MD simulations were computed using NAMD 2.13^[27] with the CHARMM36 force field^[28] for nucleic acids and ions, and the

CHARMM-modified^[29] TIP3P model^[30] for water. The van der Waals interactions were smoothly switched off in the range 8–10 Å, and the electrostatic interactions were computed without cut-off using the particle mesh Ewald method.^[31] The SHAKE and SETTLE algorithms^[32] were used to fix the length of all bonds involving hydrogen atoms with an integration time step of 2 fs. The Langevin dynamics method was used to maintain a constant temperature at 310 K, and the Nose-Hoover Langevin piston method^[33] was used to maintain a constant pressure of 1 bar in the NPT ensemble.

The angles, side lengths, volumes, and distances were measured in Pymol. For the measurements of geometric parameters, the four vertices (A, B, C, and D) of the tFNA exoskeleton were chosen (Figure 2A), and the lengths of the six sides were measured in the equilibrium state. The angles of the tFNA exoskeleton were calculated from the corresponding side lengths. The volumes were by using Euler's tetrahedron formula. The center of mass of the G-quadruplex strand, assigned as O, was calculated by a script in Pymol. The distances between O and A, B, C, and D were measured in the equilibrium state.

Fabrication of MLT-Loaded Nanobee Delivery System: The final fabrication of the MLT-loaded nanobee delivery system required four steps. First, 1 × 10⁻⁶ M AT strands were incubated with 20 × molecular excess of MLT peptides at room temperature overnight to form the compact AT/MLT core. After incubation, the core was purified by 10 kDa Amicon ultrafiltration (8000 g 3 min per run, wash with H₂O for 3 times) to remove excess oligonucleotides and peptides. The tFNA exoskeleton without the #7 strand was fabricated with the aforementioned one-pot annealing protocol. Subsequently, the AT/MLT core was mixed with the tFNA exoskeleton at a molecular ratio of 1.2:1, and slow annealing was applied from 35 to 20 °C at a ramp of 1 °C/10 min to attach the AT strand and tFNA exoskeleton via sticky end hybridization. Finally, 1 × molecular amount of strand #7 was annealed from 30 to 20 °C at a ramp of 1 °C/10 min per degree to close the exoskeleton. The final products were purified by ultrafiltration with Amicon 30 kDa 0.5 mL tubes (5000 g 5 min per run, wash with TM buffer for 3 times, Amicon Ultra 0.5 mL, 30K, cat. no. UFC503096).

Cytotoxicity Measurements: Cell apoptosis was determined using the Annexin V-FITC Apoptosis Detection Kit. HUVECs, L929 cells, and A375 cells were incubated in standard conditions before trypsin digestion. The cells were diluted to 5 × 10⁴ – 8 × 10⁴ cells mL⁻¹, plated into 6-well or 96-well plates, and incubated overnight. Subsequently, the cells were equilibrated in the medium containing 0% FBS for 1 h before further treatments. Typical treatment was incubation for 2 h with 250 × 10⁻⁹ M nanobee and MLT peptides of different concentrations. The cells were then stained using a Live/Dead kit or a CCK-8 assay kit. The cytotoxicity results were finally acquired by using a flow cytometer (Beckman, FC500) or Varioska LUX multimode microplate reader (Thermo Scientific, VL0L0TD0).

Therapeutic Evaluation of the Nanobee System: The animal experiments were approved by the Research Ethics Committee of West China Hospital of Stomatology, Sichuan University. Female BALB/c nude mice (≈20 g, 4–5 weeks old) were purchased from Gempharmatech Co., Ltd. (Nanjing, China). For generating the A375 tumor-bearing mice model, 100 μL DMEM containing A375 cells (1 × 10⁷ cells mL⁻¹) was subcutaneously injected to the left axilla of each mouse.

When the A375 tumor volume reached ≈100 mm³, the mice were randomly divided into three groups (each n = 3). Thereafter, the mice were administered with saline, 2 × 10⁻⁶ M MLT, and 1 × 10⁻⁶ M nanobee separately via tail vein injection (100 μL) every 2 days for 24 days. Tumor size and mice weight were recorded every 4 days. The tumor volume was calculated from the following equation

$$\text{Tumor volume} = 0.5 \times \text{longest diameter} \times \text{shortest diameter}^2 \quad (1)$$

The mice were imaged on the 10th and 20th day of treatment. After a 24-day treatment, mice were sacrificed and their tumors and the heart, liver, spleen, lungs, and kidneys were collected, and the tumors were imaged. The tumors and organs were fixed with 4% paraformaldehyde and stained with hematoxylin and eosin (HE) for the histopathological

evaluation. Images of samples were obtained using a microscope (Olympus, FSX100).

Supporting Information

Supporting Information is available from the Wiley Online Library or from the author.

Acknowledgements

This study was supported by National Key R&D Program of China (2019YFA0110600), National Natural Science Foundation of China (81970916, 81671031, 21834007), and Science Foundation of the Shanghai Municipal Science and Technology Commission (19JC140300 and 19PJ1404700).

Conflict of Interest

The authors declare no conflict of interest.

Keywords

DNA nanotechnology, drug delivery, framework nucleic acids, molecular dynamic analysis, nanorobotics

Received: August 28, 2020

Revised: October 10, 2020

Published online: October 28, 2020

- [1] a) S. Li, T. Tian, T. Zhang, X. Cai, Y. Lin, *Mater. Today* **2019**, *24*, 57; b) S. M. Douglas, I. Bachelet, G. M. Church, *Science* **2012**, *335*, 831; c) M. Li, H. Ding, M. Lin, F. Yin, L. Song, X. Mao, F. Li, Z. Ge, L. Wang, X. Zuo, Y. Ma, C. Fan, *J. Am. Chem. Soc.* **2019**, *141*, 18910; d) L. L. Ong, N. Hanikel, O. K. Yaghi, C. Grun, M. T. Strauss, P. Bron, J. Lai-Kee-Him, F. Schueder, B. Wang, P. Wang, J. Y. Kishi, C. Myhrvold, A. Zhu, R. Jungmann, G. Bellot, Y. Ke, P. Yin, *Nature* **2017**, *552*, 72.
- [2] a) F. Yang, Q. Li, L. Wang, G. J. Zhang, C. Fan, *ACS Sens.* **2018**, *3*, 903; b) C. Wiraja, Y. Zhu, D. C. S. Lio, D. C. Yeo, M. Xie, W. Fang, Q. Li, M. Zheng, M. Van Steensel, L. Wang, C. Fan, C. Xu, *Nat. Commun.* **2019**, *10*, 1147; c) Y. Du, P. Peng, T. Li, *ACS Nano* **2019**, *13*, 5778; d) E. Tasciotti, *Nat. Biotechnol.* **2018**, *36*, 234; e) T. Zhang, T. Tian, R. Zhou, S. Li, W. Ma, Y. Zhang, N. Liu, S. Shi, Q. Li, X. Xie, Y. Ge, M. Liu, Q. Zhang, S. Lin, X. Cai, Y. Lin, *Nat. Protoc.* **2020**, *15*, 2728.
- [3] N. Liu, X. Zhang, N. Li, M. Zhou, T. Zhang, S. Li, X. Cai, P. Ji, Y. Lin, *Small* **2019**, *15*, 1901907.
- [4] a) Y. Liu, Y. Sun, S. Li, M. Liu, X. Qin, X. Chen, Y. Lin, *Nano Lett.* **2020**, *20*, 3602; b) Y. Zhang, X. Xie, W. Ma, Y. Zhan, C. Mao, X. Shao, Y. Lin, *Nano-Micro Lett.* **2020**, *12*, 74; c) W. Ma, Y. Zhan, Y. Zhang, X. Shao, X. Xie, C. Mao, W. Cui, Q. Li, J. Shi, J. Li, C. Fan, Y. Lin, *Nano Lett.* **2019**, *19*, 4505.
- [5] S. Li, Q. Jiang, S. Liu, Y. Zhang, Y. Tian, C. Song, J. Wang, Y. Zou, G. J. Anderson, J. Y. Han, Y. Chang, Y. Liu, C. Zhang, L. Chen, G. Zhou, G. Nie, H. Yan, B. Ding, Y. Zhao, *Nat. Biotechnol.* **2018**, *36*, 258.
- [6] a) E. S. Andersen, M. Dong, M. M. Nielsen, K. Jahn, R. Subramani, W. Mamdouh, M. M. Golas, B. Sander, H. Stark, C. L. Oliveira, J. S. Pedersen, V. Birkedal, F. Besenbacher, K. V. Gothelf, J. Kjems, *Nature* **2009**, *459*, 73; b) R. Ranjbar, M. S. Hafezi-Moghadam, *Electron. Phys.* **2016**, *8*, 1857.
- [7] X. Tan, X. Lu, F. Jia, X. Liu, Y. Sun, J. K. Logan, K. Zhang, *J. Am. Chem. Soc.* **2016**, *138*, 10834.
- [8] a) S. H. Kim, K. R. Kim, D. R. Ahn, J. E. Lee, E. G. Yang, S. Y. Kim, *ACS Nano* **2017**, *11*, 9352; b) H. Ijas, I. Hakaste, B. Shen, M. A. Kostiaainen, V. Linko, *ACS Nano* **2019**, *13*, 5959; c) D. Zeng, L. San, F. Qian, Z. Ge, X. Xu, B. Wang, Q. Li, G. He, X. Mi, *ACS Appl. Mater. Interfaces* **2019**, *11*, 21859; d) X. Mao, A. J. Simon, H. Pei, J. Shi, J. Li, Q. Huang, K. W. Plaxco, C. Fan, *Chem. Sci.* **2016**, *7*, 1200.
- [9] a) S. Williams, K. Lund, C. Lin, P. Wonka, S. Lindsay, H. Yan, *Int. Workshop on DNA-Based Computers*, Springer, New York **2008**; b) D. N. Kim, F. Kilchherr, H. Dietz, M. Bathe, *Nucleic Acids Res.* **2012**, *40*, 2862.
- [10] a) W. O. Tucker, K. T. Shum, J. A. Tanner, *Curr. Pharm. Des.* **2012**, *18*, 2014; b) Q. Li, D. Zhao, X. Shao, S. Lin, X. Xie, M. Liu, W. Ma, S. Shi, Y. Lin, *ACS Appl. Mater. Interfaces* **2017**, *9*, 36695.
- [11] J. N. Zadeh, C. D. Steenberg, J. S. Bois, B. R. Wolfe, M. B. Pierce, A. R. Khan, R. M. Dirks, N. A. Pierce, *J. Comput. Chem.* **2011**, *32*, 170.
- [12] K. Sefah, D. Shangguan, X. Xiong, M. B. O'Donoghue, W. Tan, *Nat. Protoc.* **2010**, *5*, 1169.
- [13] C. M. Erben, R. P. Goodman, A. J. Turberfield, *Angew. Chem., Int. Ed. Engl.* **2006**, *45*, 7414.
- [14] J. L. Mergny, D. Sen, *Chem. Rev.* **2019**, *119*, 6290.
- [15] J. A. Mondragon-Sanchez, R. Santamaria, R. Garduno-Juarez, *Biopolymers* **2011**, *95*, 641.
- [16] H. Raghuraman, A. Chattopadhyay, *Biosci. Rep.* **2007**, *27*, 189.
- [17] M. Ogris, R. C. Carlisle, T. Bettinger, L. W. Seymour, *J. Biol. Chem.* **2001**, *276*, 47550.
- [18] a) N. R. Soman, S. L. Baldwin, G. Hu, J. N. Marsh, G. M. Lanza, J. E. Heuser, J. M. Arbeit, S. A. Wickline, P. H. Schlesinger, *J. Clin. Invest.* **2009**, *119*, 2830; b) H. Liu, Y. Hu, Y. Sun, C. Wan, Z. Zhang, X. Dai, Z. Lin, Q. He, Z. Yang, P. Huang, Y. Xiong, J. Cao, X. Chen, Q. Chen, J. F. Lovell, Z. Xu, H. Jin, K. Yang, *ACS Nano* **2019**, *13*, 12638.
- [19] R. Yazdian-Robati, P. Bayat, F. Oroojalian, M. Zargari, M. Ramezani, S. M. Taghdisi, K. Abnous, *Int. J. Biol. Macromol.* **2020**, *155*, 1420.
- [20] G. van den Bogaart, J. V. Guzman, J. T. Mika, B. Poolman, *J. Biol. Chem.* **2008**, *283*, 33854.
- [21] a) D. Shangguan, Z. Cao, L. Meng, P. Mallikaratchy, K. Sefah, H. Wang, Y. Li, W. Tan, *J. Proteome Res.* **2008**, *7*, 2133; b) H. Shi, X. He, K. Wang, X. Wu, X. Ye, Q. Guo, W. Tan, Z. Qing, X. Yang, B. Zhou, *Proc. Natl. Acad. Sci. USA* **2011**, *108*, 3900.
- [22] A. Mokhtarzadeh, H. Vahidnezhad, L. Youssefian, J. Mosafer, B. Baradaran, J. Uitto, *Trends Mol. Med.* **2019**, *25*, 1066.
- [23] A. H. Okholm, J. Kjems, *Adv. Drug Delivery Rev.* **2016**, *106*, 183.
- [24] a) M. Liu, W. Ma, Q. Li, D. Zhao, X. Shao, Q. Huang, L. Hao, Y. Lin, *Cell Proliferation* **2019**, *52*, e12511; b) L. Meng, W. Ma, S. Lin, S. Shi, Y. Li, Y. Lin, *ACS Appl. Mater. Interfaces* **2019**, *11*, 6850; c) H. Xue, F. Ding, J. Zhang, Y. Guo, X. Gao, J. Feng, X. Zhu, C. Zhang, *Chem. Commun.* **2019**, *55*, 4222.
- [25] S. Xing, D. Jiang, F. Li, J. Li, Q. Li, Q. Huang, L. Guo, J. Xia, J. Shi, C. Fan, L. Zhang, L. Wang, *ACS Appl. Mater. Interfaces* **2015**, *7*, 13174.
- [26] W. Humphrey, A. Dalke, K. Schulten, *J. Mol. Graphics* **1996**, *14*, 33.
- [27] J. C. Phillips, R. Braun, W. Wang, J. Gumbart, E. Tajkhorshid, E. Villa, C. Chipot, R. D. Skeel, L. Kale, K. Schulten, *J. Comput. Chem.* **2005**, *26*, 1781.
- [28] R. B. Best, X. Zhu, J. Shim, P. E. Lopes, J. Mittal, M. Feig, A. D. Mackerell Jr., *J. Chem. Theory Comput.* **2012**, *8*, 3257.
- [29] D. J. Price, C. L. Brooks, 3rd, *J. Chem. Phys.* **2004**, *121*, 10096.
- [30] W. L. Jorgensen, J. Chandrasekhar, J. D. Madura, R. W. Impey, M. L. Klein, *J. Chem. Phys.* **1983**, *79*, 926.
- [31] U. Essmann, L. Perera, M. L. Berkowitz, T. Darden, H. Lee, L. G. Pedersen, *J. Chem. Phys.* **1995**, *103*, 8577.
- [32] S. Miyamoto, P. A. Kollman, *J. Comput. Chem.* **1992**, *13*, 952.
- [33] a) G. J. Martyna, D. J. Tobias, M. L. Klein, *J. Chem. Phys.* **1994**, *101*, 4177; b) S. E. Feller, Y. Zhang, R. W. Pastor, B. R. Brooks, *J. Chem. Phys.* **1995**, *103*, 4613.